ACS Catalysis

Research Article

pubs.acs.org/acscatalysis

Role of Metal Coordination Structures in Enhancement of Electrocatalytic Activity of Ternary Nanoalloys for Oxygen Reduction Reaction

Bridgid N. Wanjala,[†] Bin Fang,[†] Rameshwori Loukrakpam,[†] Yongsheng Chen,*[,‡] Mark Engelhard,[§] Jin Luo,[†] Jun Yin,[†] Lefu Yang,[†] Shiyao Shan,[†] and Chuan-Jian Zhong*[,†]

[†]Department of Chemistry, State University of New York at Binghamton, Binghamton, New York 13902, United States

[‡]EMS Energy Institute, John and Willie Leone Family Department of Energy and Mineral Engineering, and Materials Research Institute, Pennsylvania State University, University Park, Pennsylvania 16802, United States

[§]EMSL, Pacific Northwest National Laboratory, Richland, Washington 99352, United States

Supporting Information

ABSTRACT: The ability to harness the metal coordination structures of nanoalloy catalysts is critical for catalyzing the oxygen reduction reaction because such a detailed atomic-scale structure dictates the surface binding site and strength for molecular oxygen and oxygenated intermediate species in the electrocatalytic process. This Article describes the results of an investigation of the metal coordination structures of ternary (PtNiCo) nanoalloys and their manipulation to enhance the electrocatalytic activity for oxygen reduction reaction. The basic hypothesis is that such atomic-scale structure can be manipulated by oxidative−reductive thermal treatment to influence the binding site and strength of molecular oxygen and oxygenated species on the nanoalloy surface. The results have revealed remarkable increases in both mass activity and specific activity for the catalysts processed by the oxidative−reductive treatment over those treated under nonreactive or low-degree oxidative atmospheres before the reductive treatment. An increased degree of heteroatomic alloying among the three metal components in the ternary catalysts and a decreased percentage of oxygenated metal species (NiO and CoO) have been revealed by X-ray absorption fine structure spectroscopy for the catalysts treated by the oxidative−reductive treatment. An enrichment of surface Pt has also been detected by X-ray photoelectron spectroscopy for such catalysts. A combination of the increase in the heteroatomic alloying, the decrease in oxygenated metal species, and the enrichment of surface Pt by the oxidative−reductive thermal treatment has therefore been concluded to be responsible for the enhanced electrocatalytic activity. The demonstration of this new approach to manipulating the metal coordination structures forms the basis for an effective strategy in engineering ternary nanoalloy catalysts, and has provided new insights into the role of such structures in the enhancement of the electrocatalytic activity.

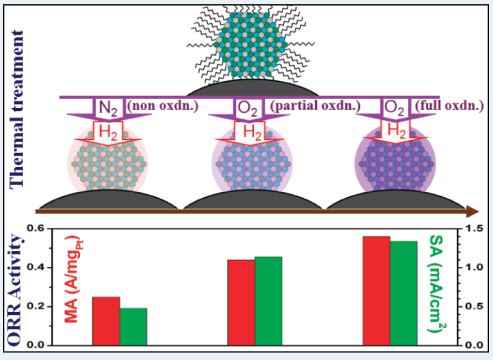

KEYWORDS: *nanoalloy, atomic-scale coordination structure, electrocatalytic activity, ternary nanoparticles, oxygen reduction reaction*

INTRODUCTION

While proton exchange membrane fuel cells promise high conversion efficiency, low pollution, and high power density for a wide range of applications, a key challenge to the ultimate commercialization of the energy conversion devices is the development of robust, active, and low-cost catalysts.[1,2] Currently, the study of Pt-based alloy catalysts for oxygen reduction reaction (ORR) is a focal point in addressing the challenge.[3−15] The enhanced electrocatalytic activity in such catalysts has been attributed to a number of factors,[16−24] including lattice,[19,20] electronic,[10,21] and Pt-skin effects.[22−24] Some of these factors can be controlled in different ways. For example, the thermal treatment can induce changes in catalyst properties such as particle size, shape, alloying degree, surface enrichment, and so forth.[18,25] Most of the studies have focused on bimetallic catalyst systems largely because of the relative simplicity in structural characterizations, whereas a limited amount of work has centered on trimetallic catalyst systems,[3−11,14,15,19,20,26−33] including our own work.[3−11,15,28−33] One group of examples of the bimetallic catalyst systems involves alloying Pt with Co or Ni, which have been the center of focus in recent years both theoretically and experimentally.[28,34−40] In comparison, several trimetallic catalysts have been shown to exhibit intriguing properties or better electrocatalytic performance than bimetallic systems. For

Special Issue: Electrocatalysis

Received: January 31, 2012
Revised: March 20, 2012
Published: April 4, 2012

example, an X-ray photoelectron spectroscopic study of carbon-supported Pt, PtCr, PtNi, PtCrCo, PtCrNi electrocatalysts prepared by coprecipitation[27] revealed that on the surface PtM/C (binary) alloy electrocatalysts are rich in Pt, whereas ternary electrocatalysts including both PtCoNi/C and PtCoCr/C happen to be rich in base metals. Among these electrocatalysts, Pt−Co/C electrocatalyst was found to possess a minimum amount of platinum oxides and thus displaying the highest electrocatalytic activity for anode reaction in direct methanol fuel cells.[27] The basic rationale for the trimetallic catalyst approach by the introduction of a second base metal to form PtMM′ (M = Ni, and M′ = Co) stems from the consideration of additional synergistic properties in terms of the formation/release of surface oxygenated species as a result of the difference in redox potentials and structural or chemical ordering/disordering because of the difference in lattice strain between M and M′, in addition to the usual benefits of PtM as known in most bimetallic approaches. This rationale has been supported by some examples of trimetallic vs bimetallic nanoparticles in the electrocatalytic ORR.[3−7,28−33] In a recent study, the electrochemical characterization and fuel-cell performance tests on a $Pt_6Ni_1Co_1/C$ catalyst prepared by the incipient wetness impregnation technique was shown to exhibit a higher electrocatalytic activity toward oxygen reduction compared with Pt/C.[19] In our recent study of carbon-supported $Pt_{36}Ni_{15}Co_{49}$ nanoparticles prepared by the molecular encapsulation method, the electrocatalytic activity for ORR was shown to be not only much higher than Pt and PtM (M = Co or Ni)[28] catalysts but also to increase with increasing thermal treatment temperature.[10] The enhanced activity has been attributed to lattice strain, in which the fcc-type lattice constant was observed to decrease with increasing thermal treatment temperature, leading to an enhanced electrocatalytic activity.

Despite these prior studies, the fundamental issue on how the metal−metal and metal−oxygen structures in the nanoscale alloy catalysts, especially for highly active ternary nanoparticle catalysts, play a role in the electrocatalytic activity has never been explicitly addressed. This issue is important because the atomic-scale metal−metal and metal−oxygen coordination structures of the nanoalloy particles dictate the binding site and strength of molecular oxygen and oxygenated intermediate species on the nanoparticle surface in the electrocatalytic process. There is therefore a clear need to develop the ability to harness the metal−metal and metal−oxygen coordination structures of the nanoalloy catalysts. Following our recent understanding of the correlation between the atomic-scale coordination structure and the electrocatalytic activity for a different trimetallic catalyst system (PtNiFe),[29] we describe herein a novel approach to the manipulation of the metal−metal and metal−oxygen coordination structures of the PtNiCo/C catalysts for the enhancement of electrocatalytic ORR activity. This approach involves thermal treatment of the nano catalysts under different atmospheres including non-reactive or minimum-reactive (N_2) and oxidative (O_2) atmospheres, followed by thermal treatment under a reductive atmosphere (H_2). A combination of techniques that measure long- and short-range order structures and surface composition, including XAFS, XRD, and XPS techniques, have been utilized to determine the metal−metal and metal−oxygen coordination structures and the relative surface structures. The results have provided fundamental insights into the role of the calcination conditions in manipulating the structure of such ternary catalysts and enabled the investigation of the role of atomic scale mixing of the components in determining ORR activity.

EXPERIMENTAL SECTION

Chemicals. Platinum(II) acetylacetonate ($Pt(acac)_2$, 97%) and nickel(II) acetylacetonate ($Ni(acac)_2$, anhydrous, >95%) were purchased from Alfar Aesar. Cobalt(III) acetylacetonate ($Co(acac)_3$, 99.95%) was purchased from Strem Chemicals, 1,2-hexadecanediol (90%), octyl ether (99%), oleylamine (70%), oleic acid (99+%), and Nafion solution (5 wt %) were purchased from Sigma-Aldrich. Optima grade perchloric acid was purchased from Fisher Scientific. Other solvents such as ethanol and hexane were purchased from Fisher Scientific. All chemicals were used as received. Water was purified with a Millipore Milli Q system.

Synthesis. The general synthesis of PtNiCo nanoparticles involved the use of three metal precursors, $Pt^{II}(acac)_2$, $Ni^{II}(acac)_2$, and $Co^{III}(acac)_3$, in controlled molar ratios. These metal precursors were dissolved in an octyl ether solvent. A mixture of oleylamine and oleic acid was added into the solution and used as capping agent. 1,2-hexadecanediol was used as a reducing agent for the reduction of the Pt-, Ni-, and Co-precursors. The synthesis of the (oleylamine/oleic acid)-capped PtNiCo nanoparticles involves the reduction reactions of the three metal precursors. The composition of the $Pt^0_{n1}Ni^0_{n2}Co^0_{n3}$ nanoparticles, where *n1*, *n2*, and *n3* represent the atomic percentages of each metal, is controlled by the feeding ratio of the metal precursors. In a typical procedure for the synthesis of $Pt_{39}Ni_{22}Co_{39}$, for example, 4.2 g of 1,2-hexadecanediol (4.88 mmol), 1.16302 g of cobalt acetylacetonate ($Co(acac)_3$, 3.26 mmol), 0.7399 g of nickel acetylacetonate ($Ni(acac)_2$, 2.88 mmol), 1.3802 g of platinum acetylacetonate ($Pt(acac)_2$, 3.51 mmol), 3 mL of oleylamine (6.4 mmol), 3 mL of oleic acid (9.4 mmol), and 450 mL of octyl ether were added to a 3-neck 1 L flask under stirring. The solution was purged with N_2 and heated to 105 °C. At this temperature, N_2 purging was stopped, and the mixture was heated to 280 °C, and refluxed for 40 min. The product was precipitated by adding ethanol. The black precipitate was completely dried under nitrogen and dispersed in a known amount of hexane.

Catalyst Preparation. The catalyst preparation included the assembly of PtNiCo nanoparticles on carbon black and subsequent thermal treatment. Briefly, 900 mg of carbon black (Ketjen Black) was suspended in 500 mL of hexane. After sonicating for ∼3 h, ∼300 mg of $Pt_{39}Ni_{22}Co_{39}$ was added into the suspension. The suspension was sonicated for 5 min, followed by stirring for ∼15 h. The powder was collected and dried under N_2. The thermal treatment involved removal of organic shells and annealing of the alloy nanoparticles. All samples were treated in a tube furnace using a quartz tube. The PtNiCo nanoparticles supported on carbon (PtNiCo/C) were first heated at 260 °C in 0−15% O_2/100−85% N_2 for 30 min for removing the organic shells, and then treated at various temperatures in the range between 400 and 926 °C in 15% H_2/85% N_2 for 120 min during the calcination process.

Measurements and Instrumentation. *Transmission Electron Microscopy.* TEM was performed on a Hitachi H-7000 electron microscope (100 kV) to obtain the particle size and its distribution. Nanoparticle samples were diluted in hexane solution and were drop cast onto a carbon-coated copper grid followed by solvent evaporation in air at room

dx.doi.org/10.1021/cs300080k | ACS Catal. 2012, 2, 795−806

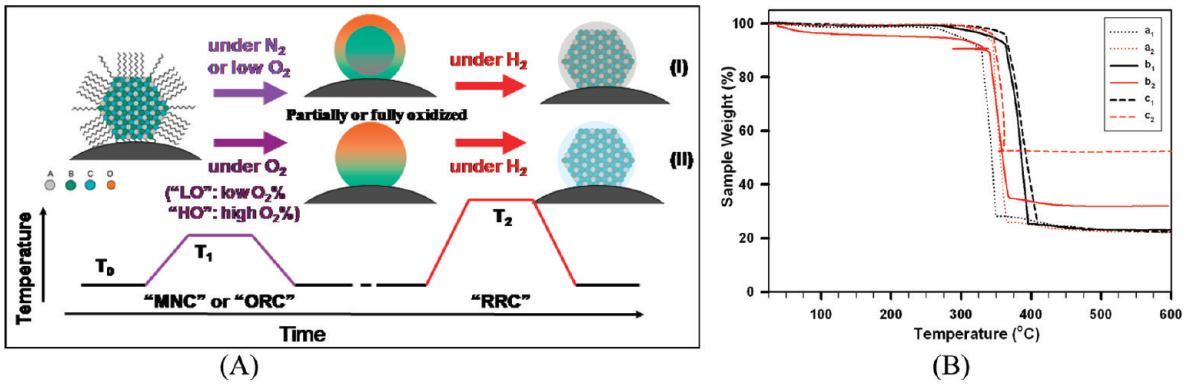

Figure 1. (A) Schematic illustration of the thermal treatment protocols of the catalyst: MNC (T_1)−RRC (T_2) and ORC (T_1, "LO" or "HO")−RRC (T_2). Typically, 1.5% O_2 refers to "LO" (i.e., low % of O_2), and 15% O_2 refers to "HO" (i.e., high % of O_2). (B) TGA curves obtained for $Pt_{25}Ni_{16}Co_{59}$/C catalysts after MNC (N_2, 260 °C) (a_1); ORC ("HO", 260 °C) (a_2); MNC (N_2, 260 °C)−RRC (400 °C) (b_1); ORC ("HO", 260 °C)−RRC (400 °C) (b_2); MNC (N_2, 260 °C)−RRC (926 °C) (c_1); ORC ("HO", 260 °C)−RRC (926 °C) (c_2).

temperature. HRTEM data were obtained using a JEOL JEM 2010F at an acceleration voltage of 200 kV.

Direct Current Plasma-Atomic Emission Spectroscopy. DCP-AES was used to analyze the composition, which was performed using an ARL Fisons SS-7 Direct Current Plasma-Atomic Emission Spectrometer. The nanoparticle samples were dissolved in concentrated aqua regia, and then diluted to concentrations in the range of 1 to 50 ppm for analysis. Calibration curves were made from dissolved standards with concentrations from 0 to 50 ppm in the same acid matrix as the unknowns. Detection limits, based on three standard deviations of the background intensity, are 20, 2, and 5 ppb for Pt, Ni, and Co. Standards and unknowns were analyzed 10 times each for 3 s counts. Instrument reproducibility, for concentrations greater than 100 times the detection limit, results in < ± 2% error.

Thermogravimetric Analysis. TGA was performed on a Perkin-Elmer Pyris 1-TGA for determining the weight of organic shell. Typical samples weighed ~4 mg and were heated in a platinum pan. Samples were heated in 20% O_2 at a rate of 10 °C/min.

X-ray Powder Diffraction. XRD was used to study the lattice constants and particle sizes of the catalysts. Powder diffraction patterns were recorded on a scintag XDS 2000 θ−θ powder diffractometer equipped with a Ge(Li) solid state detector (Cu Kα radiation). The data was collected from 2θ = 5° to 90° at a scan rate of 0.02° per step and 5 s per point.

Electrochemical Measurements. Cyclic voltammetry (CV) and rotating disk electrode (RDE) measurements were collected on two instruments. The measurements were performed using an EG&G 273 instrument or electrochemical analyzer (CHI600a, CH Instruments) in three-electrode electrochemical cells at room temperature. The polarization curves were recorded after 50 potential cycles in the range of 0.02−1.2 V with a scanning rate of 100 mV/s in a nitrogen saturated 0.1 M $HClO_4$ solution. The electrochemical active areas (ECAs) of the catalysts were obtained by integrating the charge in the H_{UPD} range in the CVs. The oxygen reduction activity was measured using RDE. The potentials are given with respect to reversible hydrogen electrode (RHE). The PtNiCo data for all compositions other than $Pt_{39}Ni_{22}Co_{39}$/C were collected on this instrument. All electrolytic (0.1 M $HClO_4$) solutions were deaerated with high purity nitrogen before CV and RDE measurements.

X-ray Absorption Fine Structure Spectroscopy. XAFS was used to determine the metal−metal and metal−oxygen coordination structures. Pt L3 edge (11,564 eV), Co K edge (7,709 eV), and Ni K edge (8,333 eV) XAFS spectra were collected on the bending magnet beamline 9-BM-B at the Advanced Photon Source, Argonne National Laboratory. A double-crystal Si (111) monochromator was used along with a Rh-coated mirror to reduce harmonics. All spectra were collected in transmission mode. Powder samples were pressed into pellets with optimal thickness to ensure good quality data. X-ray intensity before and after sample was measured by ionization chambers filled with N_2. In addition, a reference spectrum of Pt, Ni, or Co foil for energy calibration was collected simultaneously with each scan using an additional ionization chamber. XAFS can be divided into two regions, near-edge region or X-ray absorption near edge structure (XANES) and extended region (EXAFS). Processing of XANES and EXAFS data have been described and demonstrated in our previous works.[10,28,30,32] XANES spectra were processed using Athena.[41] Fitting of EXAFS spectra were performed using Artemis.[41] The fitting was limited to 2.0−16.0 $Å^{-1}$ for Pt L3 edge spectra and 2.0−12.5 $Å^{-1}$ for Ni and Co K edge spectra, using a Hanning window with dk = 1.0 $Å^{-1}$. The fits were performed to both the real and imaginary parts of $\chi(R)$ in the region of 1.0 < R < 3.2 Å. Similar analysis was also performed on reference samples of Pt, Ni, and Co foils to obtain S_0^2, the amplitude reduction factor, for the subsequent determination of the coordination numbers of the fitted structure of the samples. The S_0^2 values for Pt, Ni, and Co were determined to be 0.84, 0.81, and 0.74, respectively.

X-ray Photoelectron Spectroscopy. XPS measurements were performed to identify the oxidation states and abundance of Pt, Co and Ni on the surface of the catalysts. The XPS measurements were made by using a Physical Electronics Quantum 2000 scanning ESCA microprobe. This system uses a focused monochromatic Al Kα X-ray (1486.7 eV) source for excitation and a spherical section analyzer. The instrument has a 16-element multichannel detection system. The X-ray beam used was a 100 W, 100-μm diameter beam that was rastered over a 1.4 mm by 0.2 mm rectangle on the sample. The X-ray beam was incident normal to the sample, and the X-ray detector was at 45° away from the normal. The binding energy (BE) scale was calibrated using Cu $2p_{3/2}$ feature at 932.62 eV and Au $4f_{7/2}$ at 83.96 eV for known standards. The sample

dx.doi.org/10.1021/cs300080k | ACS Catal. 2012, 2, 795−806

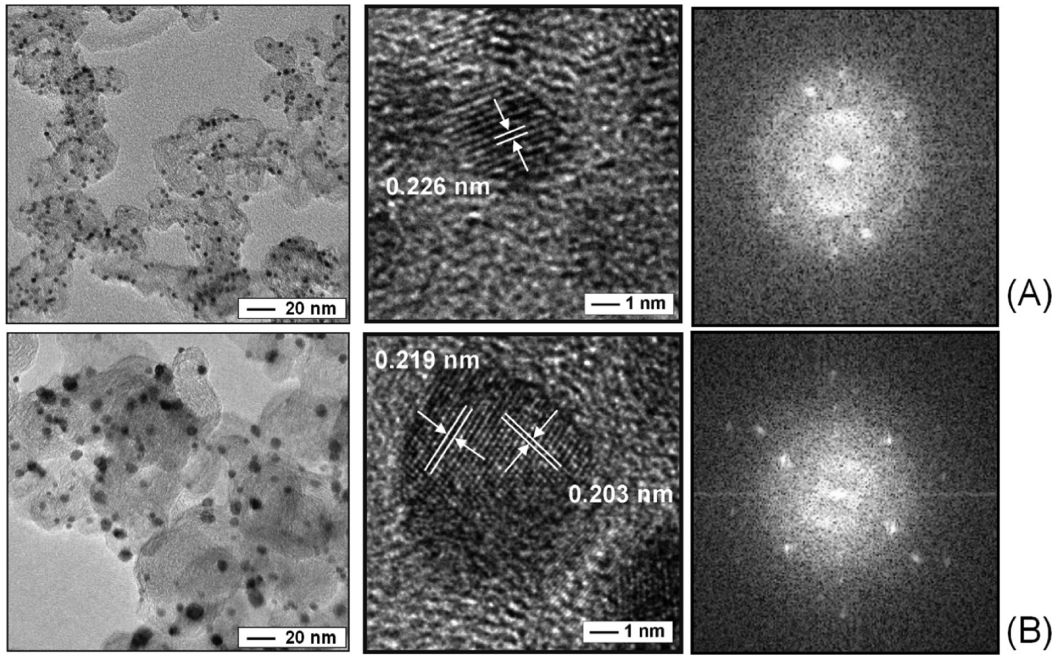

Figure 2. TEM, HRTEM, and Fast Fourier Transform (FFT) micrographs for Pt_{39} Ni_{22} Co_{39}/C catalysts after MNC (N_2, 260 °C)−RRC (H_2, 400 °C) (A) and ORC ("HO", 260 °C)−RRC (H_2, 400 °C) treatments (B). Particle sizes: 4.4 ± 0.5 nm (A) and 6.3 ± 1.2 nm (B).

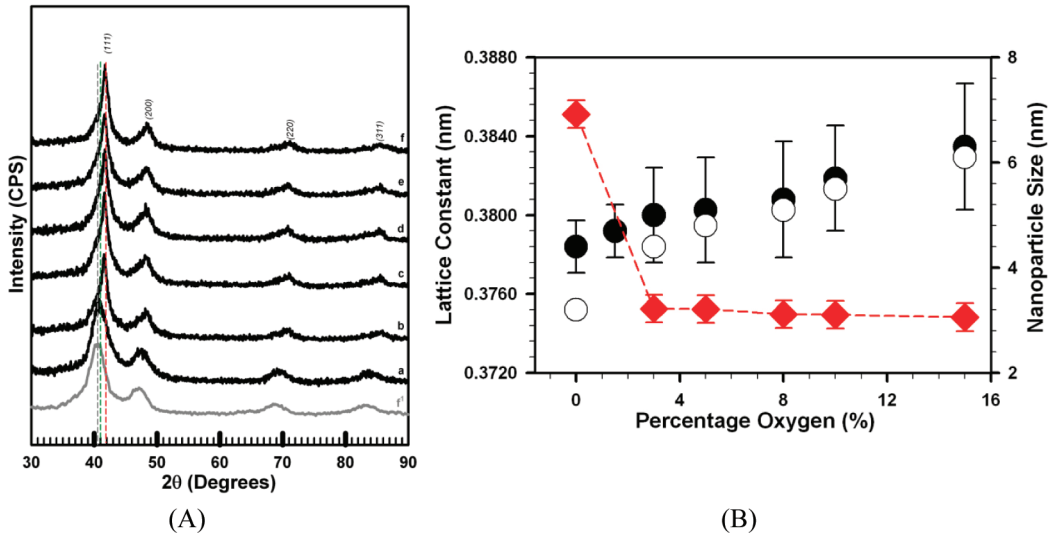

Figure 3. (A) XRD patterns for samples of $Pt_{39}Ni_{22}Co_{39}$/C catalysts as a function of O_2 percentage in ORC (0% (a), 3% (b), 5% (c), 8% (d), 10% (e), and 15% (f)) followed by RRC at 400 °C. f′ is for a catalyst treated in ORC (15% O_2) followed by RRC at 926 °C. (B) Plot of fcc-type lattice parameter (closed diamonds) and TEM size (closed circles)) and particle sizes (open circles from XRD, closed circles from TEM) as a function of O_2% in ORC.

experienced variable degrees of charging; thus, low energy electrons at ∼1 eV, 20 μA and low energy Ar^+ ions were used to minimize this charging. The percentages of individual elements detected were determined from the relative composition analysis of the peak areas.

RESULTS AND DISCUSSIONS

1. Morphological Properties. The thermal treatment of the PtNiCo/C catalysts involved heating the catalysts under oxygen (oxidative reaction condition (ORC)) or nitrogen ("minimum- or non-reactive" condition (MNC)) atmosphere to remove the capping molecules followed by hydrogen atmosphere (reductive reaction condition (RRC)) to calcine the alloy structures (Figure 1A). PtNiCo/C was heated at 260 °C in N_2 atmosphere for 30 min for the MNC treatment, or in 1.5%−15% O_2 (in N_2) for 30 min for the ORC treatment. The post ORC or MNC catalysts were then treated at 400 °C in 15% H_2 for 240 min for the RRC treatment. The complete ORC−RRC and MNC−RRC treatment sequences are illustrated in Figure 1A, where T_1 and T_2 represent the temperatures for the first treatment (i.e., MNC or ORC) and the subsequent treatment (RRC). In the ORC treatment, different O_2 concentrations were used, typically 1.5% or 15% O_2, which is labeled as "LO" (low O_2) or "HO" (high O_2).

Figure 1B shows a typical set of TGA data for $Pt_{25}Ni_{16}Co_{59}$/C nanoparticles after ORC followed by RRC at 400 or 926 °C.

dx.doi.org/10.1021/cs300080k | ACS Catal. 2012, 2, 795−806

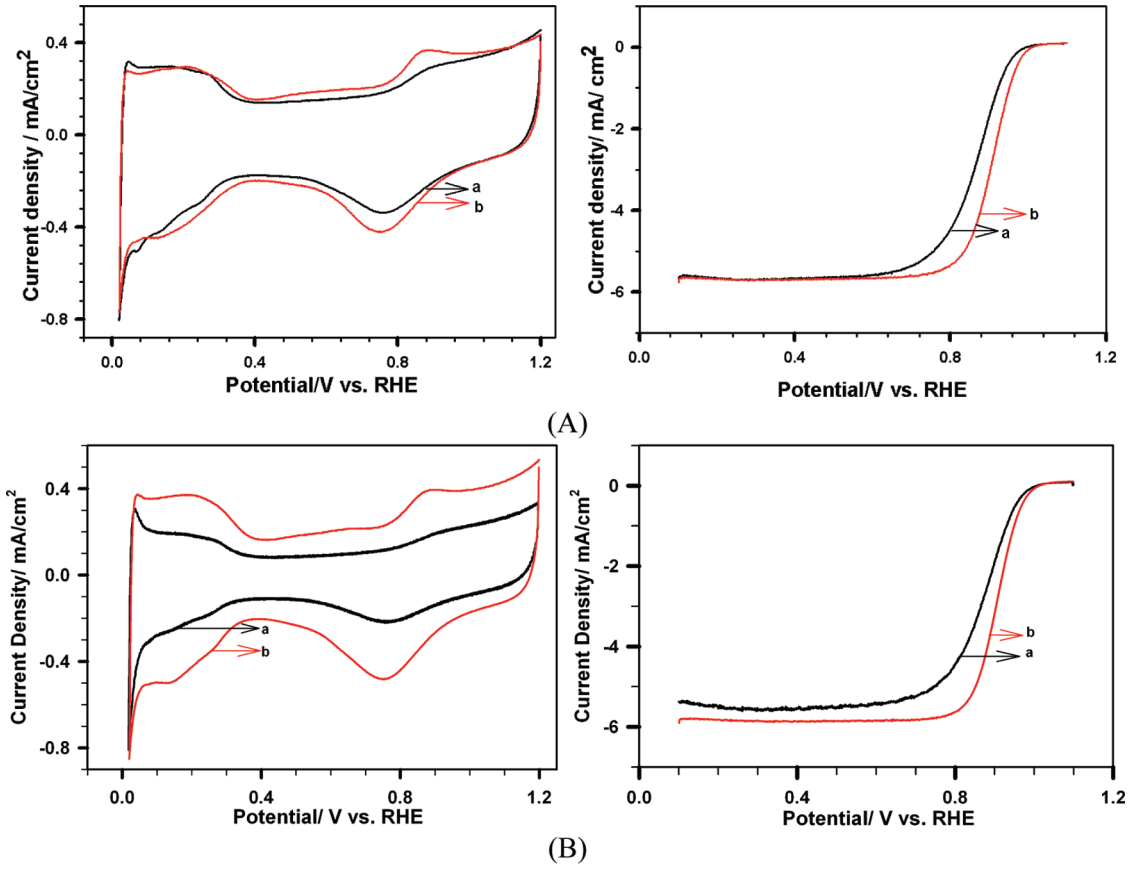

Figure 4. CV and RDE curves for (A) $Pt_{39}Ni_{22}Co_{39}$/C and (B) $Pt_{25}Ni_{16}Co_{59}$/C catalysts treated by MNC (N_2)−RRC (400 °C) (a) and ORC ("HO")−RRC (400 °C) (b). Electrolyte: 0.1 M $HClO_4$. CV curves were recorded after 10 cycles in the range of 0.02 V−1.2 V with a scan rate of 50 mV/s in nitrogen-saturated solution. RDE curves were recorded after 4 potential cycles in the range of 0.02 V−1.2 V with a scan rate of 10 mV/s at 1600 rpm in O_2-saturated solution. Catalyst loading: 10 μg on GC electrode (0.196 cm^2).

In comparison with MNC (N_2, 260 °C) treated catalyst (22% metal loading), the catalyst treated by ORC only showed no detectable changes in metal loading because of a counterbalance of removal of capping molecules and the formation of metal oxides. In comparison with MNC−RRC (400 °C) treated catalyst (22% metal loading), the catalyst treated by ORC−RRC (400 °C) showed an increase in metal loading (32% metal loading) because of burning of carbon support. In comparison with MNC−RRC (926 °C) treated catalyst (22% metal loading), the catalyst treated by ORC−RRC (926 °C) showed a large increase in metal loading (52% metal loading), indicating a significant burning effect at the higher temperature treatment.

Figure 2 shows examples of the $Pt_{39}Ni_{22}Co_{39}$/C catalysts after the MNC−RRC and ORC−RRC treatments. The TEM images and size distributions for the as-synthesized nanoparticles and the catalysts after ORC−RRC treatments with different oxygen concentrations (1−10% O_2) in the ORC are given in the Supporting Information, Figures S1−S2. When increasing the percentage of oxygen in ORC, an increase in size of the PtNiCo/C nanoparticle catalysts was observed. A similar trend of size increase with the annealing temperature was observed for a catalyst with a different composition treated under MNC−RRC condition.[10] The nanoparticles are highly crystalline, as shown by HRTEM and FFT images. In comparison with the lattice fringe for the MNC−RRC treated catalyst (0.226 nm), slightly smaller values for the ORC−RRC treated catalyst (0.219 and 0.203 nm) are observed, indicative of a mixture of (111) and (200) facets. The trend for the reduction of the lattice fringes appears to be consistent with trends of lattice constants observed using XRD technique as described next.

The catalysts were further examined by powder XRD (Figure 3A). The catalysts were subjected to thermal treatments under different percentages of oxygen used in ORC followed by RRC at 400 °C. The data reveal some significant lattice shrinking from MNC (N_2) to ORC (1.5% O_2), but insignificant change from 1.5% O_2 to 15% O_2 (Figure 3B). There is a clear decrease of lattice constant from 0.3851 nm for 0% oxygen (where 100% nitrogen treatment used for organic shell removal) to 0.3745 nm for 15%O_2 in inert atmospheres. This decrease largely occurred at <4% O_2 condition, above which the decrease is very small. This finding is in sharp contrast to the observation of a gradual decrease in the fcc-type lattice constant for PtNiCo/C catalysts treated by MNC−RRC condition as a function of the treatment temperature.[10] The lattice shrinking observed for the catalysts treated under ORC−RRC condition at 400 °C occurred largely at a few percentages of oxygen in the ORC.

The average size of the nanoparticles was also estimated utilizing the Scherrer correlation between the crystallite size (D) and the peak width (Δs, full width at half-maximum, λ = 0.154 nm for Cu Kα radiation) for Bragg diffraction. For ideal single domain crystallites, crystallite size is the same as particle diameter. For example, for the 15% O_2 treated catalyst, the calculated D value (6.1 nm) is close to the value determined from TEM data (6.3 nm) as shown in Figure 3B. The particle

dx.doi.org/10.1021/cs300080k | ACS Catal. 2012, 2, 795−806

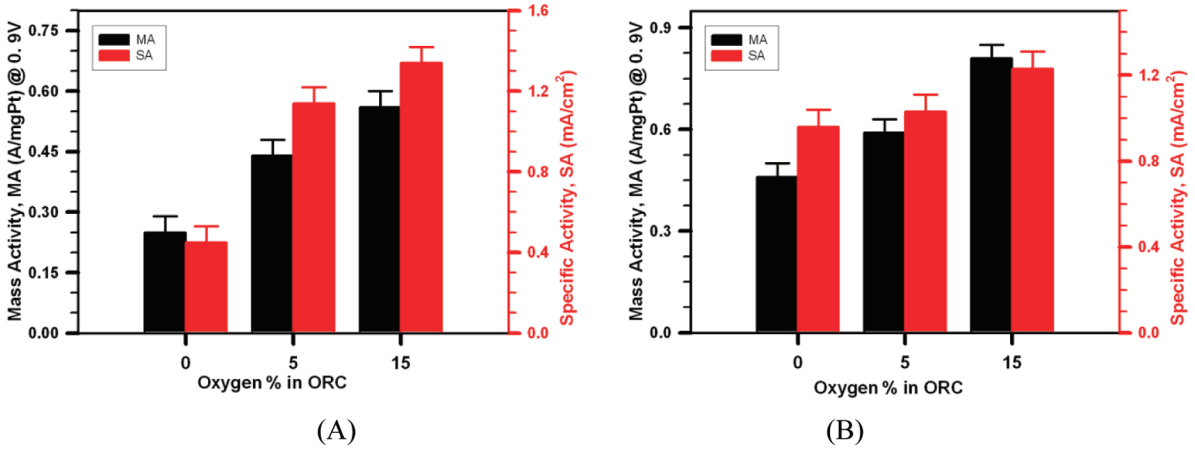

Figure 5. Comparison of mass and specific activities for $Pt_{39}Ni_{22}Co_{39}$/C (A) and $Pt_{25}Ni_{16}Co_{59}$/C (B) catalysts treated under different O_2% in ORC: 0% (i.e., MNC−RRC), ORC (5%O_2)−RRC, and ORC (15%O_2, i.e., "HO")−RRC.

sizes estimated from Scherrer equation were found to be slightly smaller than the TEM-estimated ones. Despite the small difference in the estimated sizes, a clear trend in size increase was evident by both XRD and TEM techniques. The fcc-type lattice parameters for the catalysts treated under oxygen environment were significantly smaller than those treated under nitrogen environment.[10]

2. Electrocatalytic ORR Activity. The catalysts with different compositions were studied in CV and RDE measurements. Values of the electrochemical active area (ECA), the mass activity (MA), and the specific activity (SA) extracted from the RDE and CV measurements are discussed for the catalysts of two different compositions, $Pt_{39}Ni_{22}Co_{39}$/C and $Pt_{25}Ni_{16}Co_{59}$/C. In Figure 4A, a representative set of CV data is shown for $Pt_{39}Ni_{22}Co_{39}$/C treated under MNC−RRC (A) and ORC ("HO")−RRC conditions. The characteristics in the hydrogen adsorption/desorption region show subtle dependence on the amount of oxygen. In contrast to the relatively featureless characteristic for the MNC−RRC treated catalyst, the ORC ("HO")−RRC treated catalyst shows significant peak features at 0.08−0.1 V and 0.20−0.24 V, which are associated with (110) and (100) nanocrystal facets, respectively.[42−44] The hydrogen adsorption/desorption peaks at ∼0.20 V become predominant for the oxygen treated catalyst. These differences may reflect some changes in the surface structure and electronic properties of the catalysts. By comparing the currents in the kinetic region of the RDE curves (Figure 4A), there is a clear indication of increasing kinetic current with increasing concentration of oxygen in the ORC treatment. Similar characteristics in CV and RDE data were obtained for $Pt_{25}Ni_{16}Co_{59}$/C catalysts subjected to similar treatments (Figure 4B), with subtle differences in voltammetric peaks and kinetic currents. The ECA, MA, and SA values were determined from the CV and RDE data (Supporting Information, Tables S1−S2).

In Figure 5, the mass and specific activity data are plotted as a function of oxygen concentration in ORC in the ORC−RRC treatments for $Pt_{39}Ni_{22}Co_{39}$/C (A) and $Pt_{25}Ni_{16}Co_{59}$/C (B) catalysts. There is a clear trend showing the increase of the mass activity and the specific activity with the oxygen concentration in ORC. Note that the upper limit of the oxygen concentration in the ORC for the activity increase depended on the specific catalyst composition. In most cases, the upper limit of concentration was 15−20% O_2, after which the activity showed a decrease due likely to significant burning of the carbon support materials, as suggested by the TGA data. In a few cases, this upper limit was lower than 15% O_2, suggesting differences in carbon burning for different catalysts. Nevertheless, there is a clear general trend for the increase in MA or SA by a factor of 2−3 from the MNC−RRC treated catalysts to the ORC−RRC treated catalysts.

As shown by the TGA, TEM, and XRD data, there are clear increases in particle size and metal loading from MNC−RRC to ORC−RRC. For $Pt_{39}Ni_{22}Co_{39}$/C, the particle size increased from 4.4 ± 0.5 nm for MNC−RRC to 6.3 ± 1.2 nm for ORC−RRC, and the metal loading increased from 28% to 36%. The ECA values for this set of catalysts were 51.8 and 41.6 m^2/g_{Pt}, respectively. For $Pt_{25}Ni_{16}Co_{59}$/C, the particle size increases from 3.5 ± 0.4 nm for MNC−RRC to 6.2 ± 1.1 nm for ORC−RRC, and the metal loading increases from 22% to 32%. The ECA values for this set of catalysts were 48.4 m^2/g_{Pt} and 66.4 m^2/g_{Pt}, respectively. On the basis of the particle size increase and the carbon burning induced metal loading increase, the increase of MA from MNC−RRC to ORC−RRC cannot be explained. On the other hand, the fcc-type lattice shrinking seems to provide an account to the increase of MA from MNC−RRC to ORC−RRC. However, it is still difficult to explain why the MA increases with O_2% in the ORC−RRC treatment. In our recent report,[10] there was a gradual increase of activity in connection with a gradual decrease in lattice constant with the RRC-treatment temperature for the MNC treated catalysts with a slightly different composition. In this work, while the further lattice shrinking is insignificant after ∼4% O_2 in ORC, the activity continues to increase for catalysts treated by up to ∼15% O_2. In this dependence, the degree of carbon burning showed a 10−15% increase. To further evaluate the burning effect, the RRC was performed at a much higher temperature (926 °C) for the ORC−RRC catalyst. In this case, both MA and SA were found to drop significantly, reflecting the dominance of the burning induced size increase. To understand the exact mechanistic details, the metal−metal and metal−oxygen coordination structural changes for catalysts subjected to these different thermal processing atmospheres were analyzed using XAFS and XPS techniques, as described in the next two subsections.

3. Coordination Structures of the Metals. *3. Pt-Coordination Structure.* The possible nearest neighbors around Pt include O (in Pt oxide), Pt (in Pt particle or

dx.doi.org/10.1021/cs300080k | ACS Catal. 2012, 2, 795−806

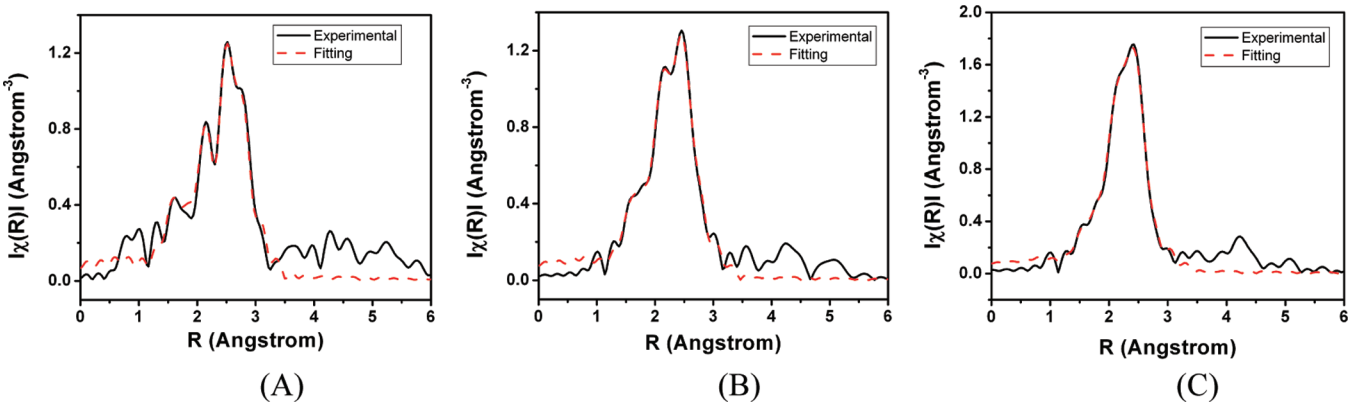

Figure 6. Original magnitude of Fourier transformed k^2-weighted Pt L3 edge EXAFS spectra of $Pt_{39}Ni_{22}Co_{39}$ catalysts after different treatments (black solid lines): ORC ("LO") (A), ORC ("LO")−RRC (B) and ORC ("HO")−RRC (C), and the corresponding fitting data (red dashed lines) using Pt−Ni model.

Table 1. Structural Parameters Obtained from Fitting of Pt L3 Edge EXAFS Data for $Pt_{39}Ni_{22}Co_{39}$/C after ORC with Different O_2% Followed by RRC at 400 °C

catalyst treatment	scattering path	*N*, coordination number	*R*, bond length (Å)	Debye−Waller factor (10^{-3} Å^2)	ΔE_0 (eV)	*R*-factor
ORC ("HO")	Pt−O	1.1 ± 0.2	1.99 ± 0.02	2.7 ± 2.5	4.4	
	Pt−Ni/Co					0.0028
	Pt−Pt	9.8 ± 0.6	2.74 ± 0.00[a]	7.1 ± 0.3	5.0	
ORC ("LO")−RRC	Pt−O	0.5 ± 0.1	1.99 ± 0.02	2.2 ± 1.8	8.4	
	Pt−Ni/Co	3.1 ± 0.3	2.61 ± 0.01	8.2 ± 0.8	6.0	0.0005
	Pt−Pt	5.4 ± 0.5	2.69 ± 0.00[a]	6.5 ± 0.3	6.0	
ORC ("HO")−RRC	Pt−O	0.3 ± 0.2	1.97 ± 0.05	3.5 ± 6.1	7.4	
	Pt−Ni/Co	4.8 ± 0.5	2.61 ± 0.00[a]	7.5 ± 0.7	6.0	0.0004
	Pt−Pt	4.9 ± 0.7	2.68 ± 0.00[a]	6.1 ± 0.5	6.0	

[a]An uncertainty of 0.00 means the value is smaller than 0.005.

Table 2. Structural Parameters Obtained from Fitting of Ni K Edge and Co K Edge EXAFS Data Using NiNi and CoCo Models for $Pt_{39}Ni_{22}Co_{39}$/C after ORC with Different O_2% Followed by RRC at 400 °C

catalyst treatment	scattering path	*N*	*R*, bond length (Å)	DWF (10^{-3} Å^2)	ΔE_0 (eV)	*R*-factor
			Ni K edge			
ORC ("HO")	Ni−O	4.7 ± 0.4	2.04 ± 0.02	5.5 ± 3.3	−5.3	0.005
	Ni−Ni[a]	13.2 ± 3.0	2.96 ± 0.01	10.1 ± 2.2	−5.3	
	Ni−Pt					
ORC ("LO")−RRC	Ni−O	2.8 ± 0.4	2.04[b]	5.5[b]	−3.4	0.022
	Ni−Ni[a]	5.9 ± 4.2	2.96[b]	10.1[b]	−3.4	
	Ni−Ni/Co	3.6 ± 1.3	2.56 ± 0.02	18.8 ± 8.8	−7.4	
	Ni−Pt	0.3 ± 1.3	2.61[c]	7.6[c]	−7.4	
ORC ("HO")−RRC	Ni−O	1.5 ± 0.4	2.04[b]	5.5[b]	−3.9	0.013
	Ni−Ni[a]	4.5 ± 2.3	2.96[b]	10.1[b]	−3.9	
	Ni−Ni/Co	1.2 ± 1.3	2.58 ± 0.02	12.6 ± 5.0	−7.9	
	Ni−Pt	3.2 ± 1.2	2.61[c]	7.1[c]	−7.9	
			Co K edge			
ORC ("HO")	Co−O	2.8 ± 0.4	1.92 ± 0.01	2.2 ± 1.8	−3.0	0.006
	Co−Co[a]	8.8 ± 2.0	2.94 ± 0.01	13.1 ± 2.6	−3.0	
ORC ("LO")−RRC(H_2)	Co−O	2.1 ± 0.2	1.92[b]	2.2[b]	−1.6	0.012
	Co−Co[a]	4.7 ± 1.1	2.94[b]	13.1[b]	−1.6	
	Co−Co/Ni	0.3 ± 1.7	2.60 ± 0.02	12.7 ± 0.9	−6.3	
	Co−Pt	3.1 ± 1.6	2.61[c]	7.6[c]	−6.3	
ORC ("HO")−RRC(H_2)	Co−O	1.1 ± 0.1	1.92[b]	2.2[b]	−1.8	
	Co−Co[a]	0.3 ± 1.3	2.94[b]	13.1[b]	−1.8	
	Co−Co/Ni	2.4 ± 1.6	2. 60 ± 0.02	12.7 ± 0.9	−6.0	
	Co−Pt	5.0 ± 1.0	2.61[c]	7.1[c]	−6.0	

[a]Second shell metal. [b]Parameters are fixed at the best values determined from their corresponding ORC ("HO") sample. [c]Parameters are fixed at the best values determined from the Pt L3 edge.

dx.doi.org/10.1021/cs300080k | ACS Catal. 2012, 2, 795−806

alloy), Ni and Co (in Pt alloy with Ni and Co). Co and Ni have very similar scattering features because of their almost identical atomic number (27 for Co and 28 for Ni) and atomic radius (the difference is about 0.007 Å). It was found that all Pt EXAFS data could be well fitted with O, Pt, Ni (PtNi model) or O, Pt, Co (PtCo model) in the first coordination shell, and the fitting results showed no significant difference in the fitted parameters within the associated uncertainties.

The original and fitted magnitude of Fourier transformed k^2-weighted Pt L3 edge EXAFS spectra and their corresponding fitted parameters using the PtNi model are presented in Figure 6 and Table 1 (see Supporting Information, Figure S3 and Table S3 for the fitting data using PtCo model). The biggest difference exists between the ORC ("HO") (i.e., ORC under high concentration of O_2 (15%)) only and the ORC−RRC treatments. No Pt−Ni/Co can be fitted for ORC (HO), indicating no or negligible formation of Pt−Ni/Co alloy without the H_2 reduction. The RRC treatment led to the reduction of Pt oxide, as shown by the significantly larger Pt−O coordination number (CN(Pt−O)) of ORC than those of ORC−RRC. In contrast, the fitted CN of Pt−Ni for ORC ("LO")−RRC and ORC ("HO")−RRC is a clear evidence of the formation of Pt−Ni/Co alloy, which also leads to a significant reduction of Pt−Pt bond distance from 2.74 Å for ORC to 2.69 Å in the presence of alloy for ORC ("LO")−RRC and 2.68 Å in the presence of alloy for ORC ("HO")−RRC catalysts.

The different oxygen treatments before the H_2 reduction apparently lead to different alloying between Pt and Ni/Co. Surprisingly, higher O_2 concentration results in better alloying. The CN(Pt−Ni/Co) increases from 3.1 ± 0.3 for ORC ("LO")−RRC to 4.8 ± 0.5 for ORC ("HO")−RRC based on the PtNi model fitting while the CN(Pt−Pt) shows a small decrease from 5.4 ± 0.5 to 4.9 ± 0.7 although the change is insignificant statistically. The small decrease or insignificant change of CN(Pt−Pt) shows that the increase in CN(Pt−Ni/Co) can not only be attributed to the growth of particle size. The increase in CN(Pt−Ni/Co) indicates better atomic level mixing of the three metals. However, the lack of a statistically significant corresponding increase in the total metal coordination (Pt−Pt plus Pt−Ni/Co) numbers, indicates that the particle size was not much larger, although according to the TEM measurements (Supporting Information, Tables S1 and S2) the particle size was slightly larger for the ORC ("HO")−RRC samples.

Comparison of the results from the two different fitting models show that regardless of fitting model, the bond distance and Debye−Waller factor of Pt−Ni/Co bond are accurately determined; thus, when later fitting Co and Ni EXAFS data, we fix the bond distance and Debye−Waller factor (DWF) of Co−Pt and Ni−Pt bonds at the values determined from Pt L3-edge EXAFS data because (1) Co−Pt and Pt−Co as well as Ni−Pt and Pt−Ni share same bond distance and DWF; and (2) because of limited available EXAFS data at Ni and Co edges bond distance and DWF of Co−Pt and Ni−Pt bonds cannot be determined accurately by fitting.

Ni and Co Coordination Structures. Global fitting was performed with Ni and Co K edge EXAFS data.[29] The fitted parameters are presented in Table 2 (see also Supporting Information, Figures S4−S7). The Ni K edge EXAFS data for ORC are well fitted with a model Ni oxide having oxygen at 2.03 Å in the first shell and Ni at 2.97 Å in the second shell (bond distances are in good agreement with that in NiO), indicating no or negligible metallic Ni in Ni particles or Pt−Ni/Co alloy without RRC. The CN(Ni−O) is significantly larger for ORC ("HO") than those for ORC−RRC. For ORC ("LO")−RRC, negligible alloying between Ni and Pt is observed (a small CN of 0.3 with overwhelming uncertainty of 1.3). In contrast, significant Ni−Pt alloying is present for higher oxygen concentration treatment as proved by the fitted CN(Ni−Pt) for ORC ("HO")−RRC (3.2 ± 1.2). Thus, a higher degree of oxidation in ORC results in better alloying between Pt and Ni after RRC. This analysis also provides a way to measure the CN of Ni around Pt, as demonstrated in our recent work.[29] Using the same approach, the CN(Pt−Ni) is found to be 0.2 (±0.7) for ORR ("LO")−RRC and 1.8 (±0.7) for ORR ("HO")−RRC (see Table 2).

Very similar to the Ni speciation, the biggest difference in Co speciation also exists between ORC and ORC−RRC. The data for ORC are very well fitted with a model Co oxide having oxygen at 1.92 Å in the first shell and Co at 2.94 Å in the second shell, indicating no or negligible metallic Co in Co particles or Pt−Ni/Co alloy. In addition, the fitted CN(Co−Pt) for the ORC−RRC is a clear evidence of the alloying between Pt and Co. The different oxygen concentration in ORC also lead to different Co−Pt alloying after RRC, as suggested by the much larger fitted CN(Co−Pt) for ORC ("HO")−RRC (5.0 ± 1.0) than that of ORC ("LO")−RRC (3.1 ± 1.6). Using the intrinsic correlation between CN(Pt−Co) and CN(Co−Pt),[29] the CN (Pt−Co) is found to be 3.1 (±1.6) for ORR("LO")−RRC and 5.0 (±1.0) for ORR("HO")−RRC catalyst (see Table 2) since there is equal amount of Pt and Co in the samples. Comparing the CN(Pt−Co) and CN(Pt−Ni), it is concluded that in ORC−RRC catalyst more Co is alloyed with Pt than Ni. This finding resonates with the observation from the Pt EXAFS data that higher O_2 concentration results in better alloying.

Ni and Co Oxide Contents in the Treated Catalysts from EXAFS. The XAFS-measured metal-O coordination number is an *average* number of oxygen over all phases in the sample. Take Ni as an example; Ni may take the following forms, Ni oxide, Ni particle, or Ni alloy. Only the Ni oxide form has nonzero oxygen coordination number. Thus, the measured CN (Ni−O), that is, the coordination number of O around Ni, can be derived as:

$$\mathrm{CN(Ni{-}O)} = \frac{\mathrm{N(Ni{-}O)}}{\mathrm{N(Ni)}} = \mathrm{N(Ni)_o} \times \frac{\mathrm{CN(Ni{-}O)_o}}{\mathrm{N(Ni)}} \quad (1)$$

where N(Ni−O) and Ni(Ni) are the numbers of Ni−O pairs and total Ni atoms in the catalyst (including all Ni forms), and $\mathrm{CN(Ni{-}O)_o}$ and $\mathrm{Ni(Ni)_o}$ are specifically the coordination number of O around Ni and the total Ni atoms in the *Ni oxide*, respectively. Thus, the proportion of Ni oxide in the catalyst, or Ni oxide content, can be calculated from eq 1 as follows:

$$\text{Ni oxide content} = \frac{\mathrm{N(Ni)_o}}{\mathrm{N(Ni)}} = \frac{\mathrm{CN(Ni{-}O)}}{\mathrm{CN(Ni{-}O)_o}} \quad (2)$$

Usually, we cannot expect the $\mathrm{CN(Ni{-}O)_o}$ of the oxide in ORC ("LO")−RRC or ORC ("HO")−RRC treated catalysts to be exactly the same as in ORC ("HO"). However, under our experimental conditions, on the outer surface of Ni oxide, Ni may well be fully coordinated with O. Thus, as a good approximation, the Ni−O CNs of the oxide in all samples are assumed to be the same. In this way the oxide content of different samples can be compared. For ORC ("HO"), EXAFS

dx.doi.org/10.1021/cs300080k | ACS Catal. 2012, 2, 795−806

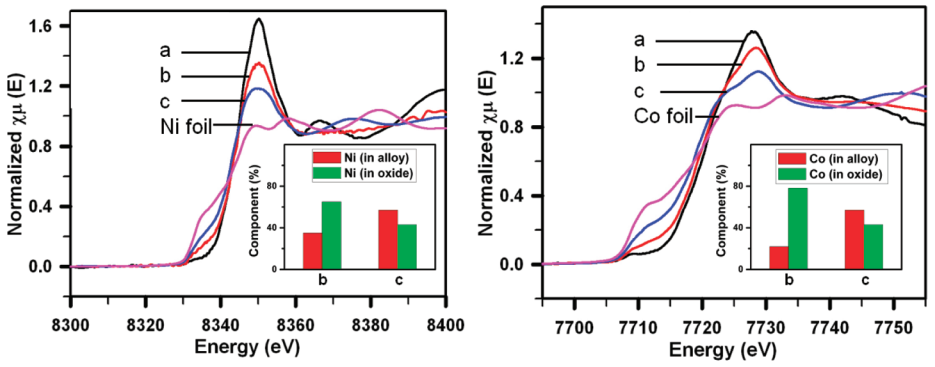

Figure 7. XANES spectra at Ni K edge (A) and Co K edge (B) for PtNiCo/C catalysts treated under ORC ("HO") (**a**), ORC ("LO")−RRC(H_2) (**b**), and ORC ("HO")−RRC(H_2) conditions (**c**). Insets: relative Ni or Co alloy (red bars) and their oxide (green bars) compositions extracted form Ni K and Co K edge data using linear combination fitting (Supporting Information, Table S4).

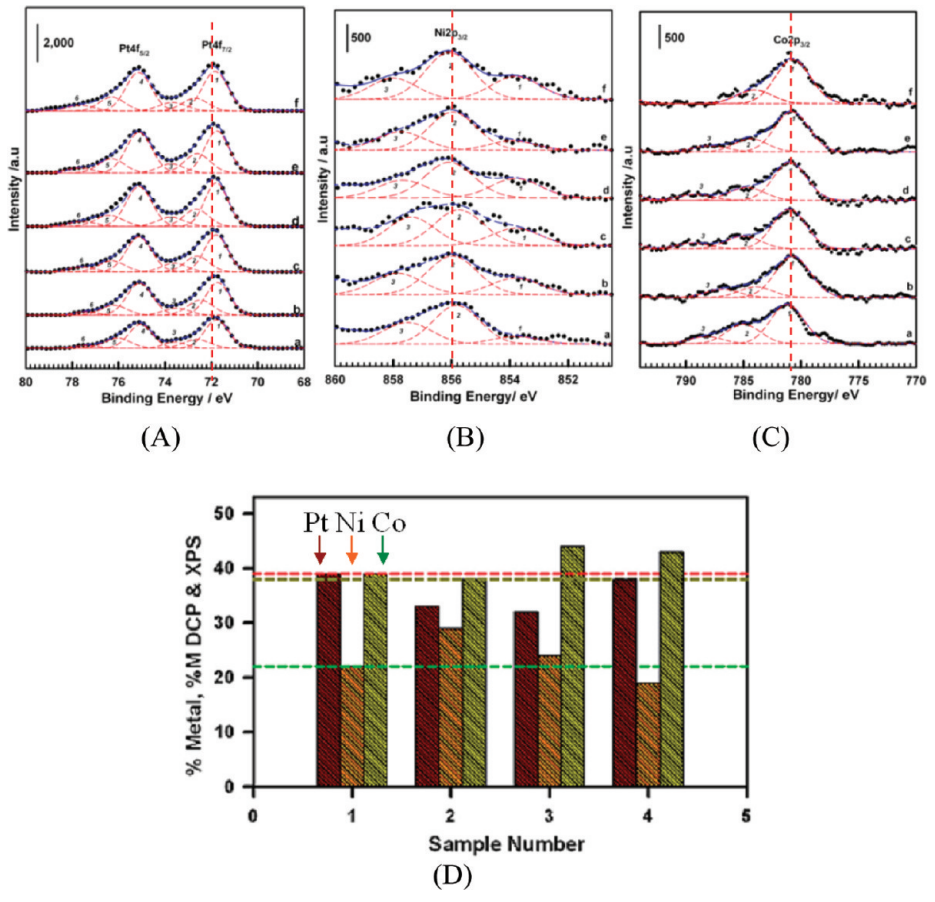

Figure 8. XPS spectra in the Pt4f (A), Ni2p (B), and Co2p (C) regions for samples of $Pt_{39}Ni_{22}Co_{39}$/C catalysts as a function of oxygen: 0% (a), 1.5% (b), 3% (c), 5% (d), 10% (e), and 15% O_2 (f) in the ORC and treated at 400 °C in the RRC (black dotted line: original curves, blue dashed lines: fitted curves; and red dashed lines: deconvoluted peaks). (D) A comparison of XPS-derived and DCP-derived atomic compositions for Pt, brown), Ni (orange) and Co (green) for samples under different states or treatments: (#1) NP from DCP, (#2) NP/C from DCP, (#3) NP/C after MNC−RRC from XPS, and (#4) NP/C after ORC ("HO")−RRC from XPS. The dashed lines show the composition of each metal for the as-synthesized nanoparticles obtained from DCP analysis.

analysis has shown that Ni is all in oxide form. Hence, its oxide content is 100%, that is, $CN(Ni{-}O)_o$ = 4.2 (see Table 2). Using eq 2 and CNs in Table 2, the Ni oxide content is determined to be 2.6/4.2 = 62% and 1.6/4.2 = 38% for ORC ("LO")−RRC and ORC ("HO")−RRC treated catalysts, respectively. The Co oxide contents are similarly obtained, yielding 83% and 50% for ORC ("LO")−RRC and ORC ("HO")−RRC treated catalysts, respectively (Supporting Information, Table S4). Note that this calculation serves as one useful estimate but is not conclusive because of the associated uncertainties and the assumptions.

Ni and Co Oxide Contents in the Treated Catalysts from XANES. Another way to estimate the oxide content of Ni or Co involves analyzing XANES spectra using the linear combination

dx.doi.org/10.1021/cs300080k | *ACS Catal.* 2012, 2, 795−806

fitting method. Take Ni again as an example. The analysis starts with identifying Ni XANES spectra that can cover major possible Ni species. Since Ni is in either oxide or alloy form, at least two components are needed for the analysis. From EXAFS measurements, it is known that Ni is in oxide form for the ORC ("HO") treated catalyst. Thus its XANES spectrum represents one component for Ni oxide in the linear combination fitting. In addition, if metallic Ni is assumed to have the same XANES spectrum as Ni foil, then only two component spectra are needed and the spectrum of Ni foil will be the other component for the fitting. Thus, the Ni oxide content in the ORC ("LO")−RRC and ORC ("HO")−RRC treated catalysts can be determined. The same procedure was also performed for Co spectral analysis. This analysis was performed with Athena[41] (see Supporting Information, Table S4). The fitting results are very close to the results derived from the EXAFS data. In comparison with predominant metal oxides in the ORC only, the ORC−RRC treated catalysts showed a significant reduction of metal oxides. The detected metal oxides were due to exposure of the catalysts to ambient conditions after the treatment. As shown in Figure 7, it is evident that less Ni and Co oxides were observed from XANES data for the ORC ("HO")−RRC in comparison with the ORC ("LO")−RRC, indicating an important role played by preoxidation of the nanoalloy. The increase of the O_2 concentration in the ORC led to a clear increase of Ni (or Co) in the alloys and reduction of NiO and CoO oxides (Figure 7 inset). The detected changes in coordination numbers translate to an increased alloying degree and a decreased oxide (NiO_x and CoO_y) formation for the treatment under an increased O_2%. Note that the above estimate of the Ni and Co oxide contents is not conclusive due the associated uncertainty (see Supporting Information). Nevertheless, there is a relative change of the Ni and Co oxide species in the catalysts that were exposed to ambient condition after the treatments. The amount of oxide species of these elements is directly related to the change of the extent of alloying. It is the extent of alloying of the Ni and/or Co with the Pt that has played a major role in determining the difference in the catalytic activities of these catalysts.

In summary, there are several key findings from XAFS. First, the CNs of Pt−Ni for ORC ("LO")−RRC (Pt−Ni/Co CN = 2.9) and ORC ("HO")−RRC (Pt−Ni/Co CN = 4.5) are clearly indicative of the formation of Pt−Ni/Co alloy, which also leads to a reduction of Pt−Pt bond distance from 2.74 Å for ORC (Pt particle core) to 2.69 Å for ORC ("LO")−RRC and 2.68 Å for ORC ("HO")−RRC. The high oxygen content in the ORC results in better alloying between Pt and Ni/Co upon the RRC treatment, and more Co than Ni alloys with Pt partly because there is more Co than Ni in the samples. In addition, there is a significant decrease in oxide content (see Supporting Information for their estimation) for the ORC with a higher %O_2, which may play a role in the enhanced activity of the ORC ("HO")−RRC over ORC ("LO")−RRC or MNC−RRC catalysts.

4. Relative Surface Composition. The question on how the above changes are linked to the changes in the surface composition was examined using the XPS technique. On the basis of the asymmetric shapes of the spectra in the Pt 4f, Ni 2p, and Co 2p regions, there are apparently components corresponding to higher oxidation states. As shown by spectral deconvolution of Pt(4f), Co($2p_{3/2}$), and Ni ($2p_{3/2}$) in Figure 8A−C (and Supporting Information, Table S5), Pt, Ni, and Co with different oxidation states were clearly detected, which correspond to surface oxides of these metals, in qualitative agreement with the data from the XANES spectra.

The BE values for Pt $4f_{7/2}$, Ni $2p_{3/2}$, and Co $2p_{3/2}$ are practically identical for the $Pt_{39}Ni_{22}Co_{39}$/C and treated catalysts. However, there is a significant difference between the individual BE values for as-synthesized PtNiCo nanoparticles and carbon supported/calcined counterparts of the same composition. For example, the Pt^0 $4f_{7/2}$ bands were observed at 71.7 to 71.8 eV for the $Pt_{39}Ni_{22}Co_{39}$/C samples loaded on carbon and treated under different conditions of oxygen (0−15%) followed by hydrogen treatment at 400 °C (Figure 8A). The Co^0 $2p_{3/2}$ peaks are in the range of 780.7−780.9 eV for $Pt_{39}Ni_{22}Co_{39}$/C treated under different conditions of oxygen and annealed at 400 °C (Figure 8B). However, the Ni^0 $2p_{3/2}$ peaks were observed in the range of 853.8 to 853.9 eV (Figure 8C) for $Pt_{39}Ni_{22}Co_{39}$/C and treated under different conditions of oxygen and annealed at 400 °C. The systematic shift in Pt4f, Ni2p, and Co2p peak positions after thermal treatment could be due to the support and enhanced alloying effect.

For $Pt_{39}Ni_{22}Co_{39}$ catalyst treated by ORC at different O_2%, the compositions determined from the XPS data yielded variable compositions ($Pt_{30-38}Ni_{19-25}Co_{42-45}$) (Figure 8D and Supporting Information, Table S6). The difference between the bulk analysis data and the surface analysis data was significant particularly for Co species whose XPS composition was found to be significantly higher for all ORC-treated samples. By comparing with the MNC−RRC treated catalyst, there is an observable increase of Pt at the expense of Ni and Co for the ORC ("HO")−RRC catalyst which showed a composition of "$Pt_{38}Ni_{19}Co_{43}$", suggesting surface enrichment of Pt. At >10% O_2, the detected Pt increases close to the bulk composition as determined from DCP-AES analysis (Supporting Information, Figure S8A). Similar trends with subtle differences were also observed for other catalyst compositions such as $Pt_{18}Ni_{23}Co_{59}$/C treated at 400 °C, and $Pt_{36}Ni_{15}Co_{49}$/C treated by different temperatures (Supporting Information, Figure S9, Table S6). For the temperature dependency study under N_2 and hydrogen treatment conditions, there was no significant difference between the bulk and surface compositions. However, in the presence of oxygen and lower temperature treatment under reductive annealing conditions, a surface enrichment phenomenon could occur, resulting in a surface that was base metal rich (Co and Ni) or Pt metal rich depending on the actual composition. The difference between the bulk and surface analysis data was significant particularly for Co species whose XPS composition was found to be significantly higher for all oxygen treatment conditions.

The correlation of the relative change in the amount of surface oxide species with the percentage of oxygen used in the ORC was also examined. The XPS analysis results (Supporting Information, Figure S8B) showed a clear decrease in the amount of detected oxygen from MNC−RRC to ORC−RRC with increasing O_2% in the ORC. It decreased from 11% for the MNC−RRC catalyst to 7% for the ORC (10−15%O_2)−RRC catalysts. While the decrease could in part reflect the particle size growth under ORC condition, the difference of the detected oxygen between the MNC−RRC and ORC−RRC catalysts is clearly consistent with the EXAFS/XANES analysis results, confirming that the O-species originate largely from the nanoparticle surfaces. The significant difference in terms of the relative surface element enrichment between the catalysts treated under the two different gas environments is believed to

dx.doi.org/10.1021/cs300080k | ACS Catal. 2012, 2, 795−806

reflect the impact of surface oxide formed in the ORC treatment to the metal alloying and atomic redistribution upon the subsequent RRC treatment environment as revealed by the XAFS data analysis. There is a relative enrichment of surface Pt over Ni/Co on the ORC−RRC catalyst in comparison with MNC−RRC catalyst.

CONCLUSIONS

Taken together, the observed enhancement of the electrocatalytic activity by the controlled ORC−RRC treatment can be attributed to combination of metal−metal and metal−oxygen coordination structures and their surface redistributions (Scheme 1). The metal−metal and metal−oxygen coordination structures reconstruct in the RRC toward a higher degree of alloying in the nanoparticle and a lower propensity of metal oxidation on the surface. This process is also accompanied by enrichment of Pt on the surface at the expense of Ni or Co. The higher degree of alloying favors the reduction of the fcc-type Pt−Pt lattice distances, which together with the surface enriched Pt, enhances the activation of the molecular oxygen. The reduced propensity of surface oxidation favors the availability of surface sites for removing oxygenated species adsorbed on the Pt sites following the reduction of molecular oxygen. Both the mass activity and the specific activity for the catalysts treated under oxygen atmosphere in the ORC−RRC treatment were found to increase by a factor of 2−3 in comparison with those treated under nitrogen in the MNC−RRC treatment. In addition to the decrease of the fcc-type lattice parameter, a higher percentage of alloys and lower percentages of surface oxides is found for the catalysts treated under a higher oxygen atmosphere in the ORC−RRC treatment than those treated under nitrogen or traces of oxygen followed by RRC treatment. The catalysts treated under a higher oxygen atmosphere in the ORC exhibit a lower Ni−O/Co−O coordination number and an enrichment of surface Pt than those treated under nitrogen or traces of oxygen in the MNC or ORC before the RRC treatment. A combination of the increase in the alloying degree, the decrease in oxide content, and the enrichment of surface Pt for the catalysts treated by the oxidative−reductive thermal processing has been concluded to be responsible for the enhanced electrocatalytic activity for ORR. The reconstruction of the alloy in the oxidative−reductive thermal processing provides new insights into the role of metal−metal and metal−oxygen coordination structures in the enhancement of the electrocatalytic activity.

We note that while the most active catalyst is shown to consist of Pt rich PtNiCo alloy with the excess Ni and Co present as oxygenated metal species or oxides, this conclusion can only apply to the structure of the catalyst before the electrochemical test. The data do not provide information concerning the change of the surface composition upon exposing the catalyst to the acidic electrolyte for the electrochemical test. In the acidic electrolyte, the surface oxides could dissolve, leaving only a reconstructed alloy surface behind. Different nanoalloys may undergo different surface reconstruction upon exposing to the acidic electrolyte. How the change of the surface composition correlates to the structure of the as-prepared/as-processed catalyst is yet to be determined, which is part of our further investigation that will involve the use of in situ spectroscopic-electrochemical techniques.

Scheme 1. ORR Electrocatalytic Activity of the Trimetallic Catalysts (bottom panel) as a Function of the Degree of Oxidation Treatment in the ORC Process ("non oxdn", "partial oxdn", and "full oxdn" in the scheme represent non oxidation, partial oxidation, and full oxidation treatments, respectively), Followed by the Controlled RRC Treatment (top panel), and Are Correlated with a Combination of Metal−Metal and Metal−Oxygen Coordination Structures and Their Surface Redistributions

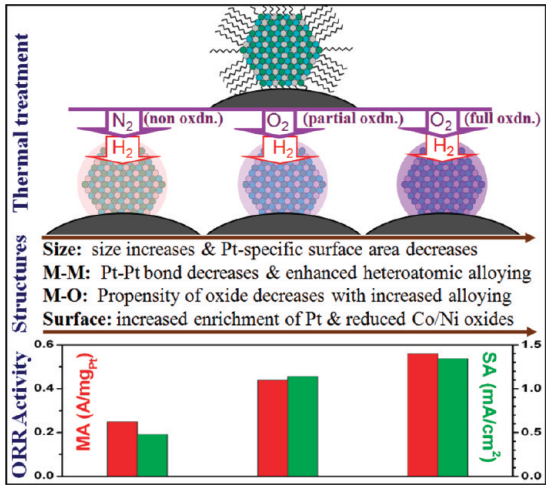

ASSOCIATED CONTENT

Supporting Information

Additional TEM, XAFS, and XPS data. This material is available free of charge via the Internet at http://pubs.acs.org.

AUTHOR INFORMATION

Corresponding Author

*E-mail: cjzhong@binghamton.edu (C.-J.Z.), yzc2@psu.edu (Y.C.).

Funding

This work was supported by the National Science Foundation (CBET-0709113, CHE 0848701). The work was also in part supported by DOE-BES (DE-SC0006877). The XAFS work at the 9-BM Beamline was supported in part by the Office of Basic Energy Sciences of the U.S. Dept. of Energy and by the National Science Foundation Division of Materials Research. Use of the Advanced Photon Source is supported by the Office of Basic Energy Sciences of the U.S. Department of Energy under Contract No. W-31-109-Eng-38. The XPS measurement was performed using EMSL, a national scientific user facility sponsored by the Department of Energy's Office of Biological and Environmental Research located at Pacific Northwest National Laboratory.

Notes

The authors declare no competing financial interest.

ACKNOWLEDGMENTS

We thank Dr. I-T Bae for assistance in HR-TEM analysis, and Dr. H. R. Naslund for assistance in DCP-AES analysis.

REFERENCES

(1) Gasteiger, H. A.; Kocha, S. S.; Sompalli, B.; Wagner, F. T. *Appl. Catal., B* **2005**, *56*, 9−35.

(2) Mallouk, T. E. Smotkin, E. S. Combinatorial catalyst development methods. In *Handbook of Fuel Cells−Fundamentals, Technology and*

Application; Vielstich, W., Lamm, A., Gasteiger, H. A., Eds.; John Wiley & Sons: New York, 2003.
(3) He, T.; Zhong, C. J.; Luo, J.; Maye, M. M.; Han, L.; Kariuki, N. N.; Wang,, L. U.S. Patent 7,335,245, 2008.
(4) He, T.; Kreidler, E.; Xiong, L.; Luo, J.; Zhong, C. J. *J. Electrochem. Soc.* **2006**, *153*, A1637−A1643.
(5) Luo, J.; Han, L.; Kariuki, N. N.; Wang, L. Y.; Mott, D.; Zhong, C. J.; He, T. *Chem. Mater.* **2005**, *17*, 5282−5290.
(6) Luo, J.; Kariuki, N.; Han, L.; Wang, L. Y.; Zhong, C. J.; He, T. *Electrochim. Acta* **2006**, *51*, 4821−4827.
(7) Luo, J.; Wang, L. Y.; Mott, D.; Njoki, P. N.; Kariuki, N.; Zhong, C. J.; He, T. *J. Mater. Chem.* **2006**, *16*, 1665−1673.
(8) Zhong, C. J.; Luo, J.; Njoki, P. N.; Mott, D.; Wanjala, B.; Loukrakpam, R.; Lim, S.; Wang, L.; Fang, B.; Xu, Z. C. *Energy Environ. Sci.* **2008**, *1*, 454−466.
(9) Zhong, C. J.; Luo, J.; Fang, B.; Wanjala, B. N.; Njoki, P. N.; Loukrakpam, R.; Yin, J. *Nanotechnology* **2010**, *21*, 062001.
(10) Wanjala, B. N.; Loukrakpam, R.; Luo, J.; Njoki, P. N.; Mott, D.; Zhong, C. J.; Shao, M.; Protsailo, L.; Kawamura, T. *J. Phys. Chem. C* **2010**, *114*, 17580−17590.
(11) Fang, B.; Luo, J.; Njoki, P. N.; Loukrakpam, R.; Mott, D.; Wanjala, B.; Hu, X.; Zhong, C. J. *Electrochem. Commun.* **2009**, *11*, 1139−1141.
(12) Gasteiger, H. A.; Markovic, N. M. *Science* **2009**, *324*, 48−49.
(13) Jeon, M. K.; McGinn, P. J. *J. Power Sources* **2009**, *194*, 737−745.
(14) Jeon, M. K.; Cooper, J. S.; McGinn, P. J. *J. Power Sources* **2009**, *192*, 391−395.
(15) Wanjala, B. N.; Luo, J.; Loukrakpam, R.; Fang, B.; Mott, D.; Njoki, P. N.; Engelhard, M.; Naslund, H. R.; Wu, J. K.; Wang, L. C.; Malis, O.; Zhong, C. J. *Chem. Mater.* **2010**, *22*, 4282−4294.
(16) Mott, D.; Luo, J.; Njoki, P. N.; Lin, Y.; Wang, L. Y.; Zhong, C. J. *Catal. Today* **2007**, *122*, 378−385.
(17) Luo, J.; Njoki, P. N.; Lin, Y.; Wang, L. Y.; Zhong, C. J. *Electrochem. Commun.* **2006**, *8*, 581−587.
(18) Bezerra, C. W. B.; Zhang, L.; Liu, H. S.; Lee, K. C.; Marques, A. L. B.; Marques, E. P.; Wang, H. J.; Zhang, J. J. *J.Power Sources* **2007**, *173*, 891−908.
(19) Seo, A.; Lee, J.; Han, K.; Kim, H. *Electrochim. Acta* **2006**, *52*, 1603−1611.
(20) Antolini, E. *Appl. Catal., B* **2007**, *74*, 337−350.
(21) Mukerjee, S.; Srinivasan, S.; Soriaga, M. P.; McBreen, J. *J. Phys. Chem.* **1995**, *99*, 4577−4589.
(22) Stamenkovic, V.; Schmidt, T. J.; Ross, P. N.; Markovic, N. M. *J. Phys. Chem. B* **2002**, *106*, 11970−11979.
(23) Stamenkovic, V. R.; Mun, B. S.; Mayrhofer, K. J. J.; Ross, P. N.; Markovic, N. M. *J. Am. Chem. Soc.* **2006**, *128*, 8813−8819.
(24) Stamenkovic, V. R.; Mun, B. S.; Arenz, M.; Mayrhofer, K. J. J.; Lucas, C. A.; Wang, G. F.; Ross, P. N.; Markovic, N. M. *Nat. Mater.* **2007**, *6*, 241−247.
(25) Koh, S.; Toney, M. F.; Strasser, P. *Electrochim. Acta* **2007**, *52*, 2765−2774.
(26) Jalan, V. M. U.S. Patent 5,079,107, 1992.
(27) Shukla, A. K.; Neergat, M.; Bera, P.; Jayaram, V.; Hegde, M. S. *J. Electroanal. Chem.* **2001**, *504*, 111−119.
(28) Loukrakpam, R.; Luo, J.; He, T.; Chen, Y.; Xu, Z.; Njoki, P. N.; Wanjala, B. N.; Fang, B.; Mott, D.; Yin, J.; Klar, J.; Powell, B.; Zhong, C. J. *J. Phys. Chem. C* **2011**, *115*, 1682−1694.
(29) Wanjala, B. N.; Fang, B.; Luo, J.; Chen, Y.; Yin, J.; Engelhard, M.; Loukrakpam, R.; Zhong, C. J. *J. Am. Chem. Soc.* **2011**, *133*, 12714−12727.
(30) Loukrakpam, R.; Wanjala, B. N.; Yin, J.; Fang, B.; Luo, J.; Chen, Y.; Petkov, V.; Zhong, C. J.; Shao, M.; Protsailo, L.; Kawamura, T. *ACS Catal.* **2011**, *1*, 562−572.
(31) Fang, B.; Wanjala, B. N.; Yin, J.; Loukrakpam, R.; Luo, J.; Hu, X.; Last, J.; Zhong, C. J. *Int. J. Hydrogen Energy* **2012**, *37*, 4627−4632.
(32) Fang, B.; Luo, J.; Chen, Y.; Wanjala, B. N.; Loukrakpam, R.; Hong, J.; Yin, J.; Hu, X.; Hu, P.; Zhong, C. J. *ChemCatChem* **2011**, *3*, 583−593.
(33) Fang, B.; Luo, J.; Njoki, P. N.; Loukrakpam, R.; Wanjala, B.; Hong, J.; Yin, J.; Hu, X.; Last, J.; Zhong, C. J. *Electrochim. Acta* **2010**, *55*, 8230−8236.
(34) Norskov, J. K.; Rossmeisl, J.; Logadottir, A.; Lindqvist, L.; Kitchin, J. R.; Bligaard, T.; Jonsson, H. *J. Phys. Chem. B* **2004**, *108*, 17886−17892.
(35) Stamenkovic, V.; Mun, B. S.; Mayrhofer, K. J. J.; Ross, P. N.; Markovic, N. M.; Rossmeisl, J.; Greeley, J.; Norskov, J. K. *Angew. Chem., Int. Ed.* **2006**, *45*, 2897−2901.
(36) Xu, Y.; Ruban, A. V.; Mavrikakis, M. *J. Am. Chem. Soc.* **2004**, *126*, 4717−4725.
(37) Stamenkovic, V. R.; Fowler, B.; Mun, B. S.; Wang, G. F.; Ross, P. N.; Lucas, C. A.; Markovic, N. M. *Science* **2007**, *315*, 493−497.
(38) Chen, S.; Sheng, W. C.; Yabuuchi, N.; Ferreira, P. J.; Allard, L. F.; Shao-Horn, Y. *J. Phys. Chem. C* **2009**, *113*, 1109−1125.
(39) Fowler, B.; Lucas, C. A.; Omer, A.; Wang, G.; Stamenkovic, V. R.; Markovic, N. M. *Electrochim. Acta* **2008**, *53*, 6076−6080.
(40) Wu, J. B.; Zhang, J. L.; Peng, Z. M.; Yang, S. C.; Wagner, F. T.; Yang, H. *J. Am. Chem. Soc.* **2010**, *132*, 4984−4985.
(41) Ravel, B.; Newville, M. *J. Synchrotron Radiat.* **2005**, *12*, 537−541.
(42) Wang, C.; Daimon, H.; Lee, Y.; Kim, J.; Sun, S. *J. Am. Chem. Soc.* **2007**, *129*, 6974−6975.
(43) Chen, J. Y.; Lim, B.; Lee, E. P.; Xia, Y. N. *Nano Today* **2009**, *4*, 81−95.
(44) Zhou, H. J.; Zhou, W. P.; Adzic, R. R.; Wong, S. S. *J. Phys. Chem. C* **2009**, *113*, 5460−5466.